

# PHASE RETRIEVAL WITH BACKGROUND COMPENSATION IN 4F CONFIGURATION: ADVANCED AUGMENTED LAGRANGIAN TECHNIQUE FOR AMPLITUDE OBJECT

Artem Migukin,<sup>1\*</sup> Mostafa Agour<sup>2,3</sup> and Vladimir Katkovnik<sup>1</sup>

<sup>1</sup> *Department of Signal Processing, Tampere University of Technology, FI-33101 Tampere, Finland*

<sup>2</sup> *Bremer Institut für angewandte Strahltechnik, Klagenfurter Str. 2, D-28359 Bremen, Germany*

<sup>3</sup> *Physics Department, Faculty of Science, Aswan University, 81528 Aswan, Egypt*

\* *Corresponding author: artem.migukin@tut.fi*

## ABSTRACT

Generally, wave field reconstructions obtained by phase-retrieval algorithms are noisy, blurred and corrupted by various artifacts such as irregular waves, spots, etc. These disturbances, arising due to many factors such as non-idealities of optical system (misalignment, focusing errors), dust on optical elements, reflections, vibration, are hard to be localized and specified. It is assumed that there is a generalized pupil function at the object plane which describes aberrations in the coherent imaging system manifested at the sensor plane. Here we propose a novel two steps phase-retrieval algorithm to compensate these distortions. We first estimate the cumulative disturbance, called “background”, using special calibration experiments. Then, we use this background for reconstruction of the object amplitude and phase. The second part of the algorithm is based on the maximum likelihood approach and, in this way, targeted on the optimal amplitude and phase reconstruction from noisy data. Numerical experiments demonstrate that the developed algorithm enables the compensation of various typical distortions of the optical track so sharp object imaging for a binary test-chart can be achieved.

**Index Terms**— Noise in imaging systems, Spatial light modulators, Phase retrieval, Inverse problems

## 1. INTRODUCTION

The phase contains important information on the shape of the object, which is useful in metrology and 3D imaging, e.g. microscopy, astronomy, material analysis, etc. The conventional sensors detect only the intensity of the light. Since the phase cannot be measured directly and it is systematically lost in observations, computational phase recovering techniques are

required for imaging and data processing. Phase recovering and, in general, the reconstruction of the object amplitude and phase is referred to as the phase-retrieval problem.

Perhaps the first iterative method for phase retrieval from intensity measurements were the well-known Gerchberg–Saxton algorithm [1], initially for a single observation plane, and its variation devised by Misell [2] for two defocusing images at different measurement planes. The idea consisting in the iterative replacement of the estimated magnitude by measured and prior information is further developed for various applications by many authors (e.g. [3, 4, 5, 6]). Similar methods are proposed for Fresnel instead of Fourier transforms as the transfer functions of the wave field propagation [7, 8, 9]. Various phase-retrieval algorithms based on these landmark works are systematized by Fienup [10] introducing classical types of iterative phase-retrieval algorithms. Multiple measurements gain an observation redundancy that can be exploited in order to improve the quality of the complex-valued object reconstruction [11, 12, 13].

The above imaging techniques are mainly based on an *ideal* wave field propagation modeling derived from the scalar diffraction theory [14]. In practice, wave fields in real coherent imaging systems and their observations are quite different from those predicted by theory, hence wave field reconstructions obtained by simulations (i.e. theoretical results) and using real experimental data can dramatically vary. The reconstructions obtained from the real data differ from simulated ones by multiple and well seen artifacts which can have a form of disturbed background with irregular waves, spots, random noise, etc. These systematic distortions appear due to many factors such as non-idealities of optical system (misalignment, focusing errors, aberrations), dust on optical elements, reflections, vibration, etc.

In this paper we consider a 4f optical system with an SLM located across the Fourier domain of the first lens. This system is used for capturing multiple intensity observations at the sensor plane for the phase reconstruction (see Fig. 1, [15]). The reconstruction from this data is very sensitive to all disturbing factors because it is an ill-posed problem. One of the

This work was supported by the Academy of Finland: project no. 138207, 2011–2014. The postgraduate work of Artem Migukin is funded by Tampere Doctoral Programme in Information Science and Engineering (TISE). Mostafa Agour gratefully acknowledge the financial support of the Deutsche Forschungsgemeinschaft (DFG) for funding a part of this work within the frame of the project DynaLiFeS (BE1924/2-1).

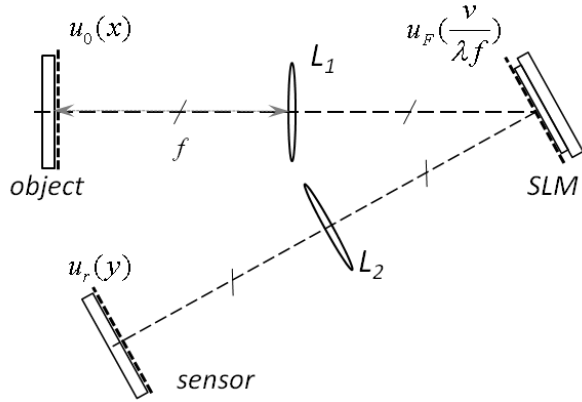


**Fig. 1.** Experimental setup of the 4f optical system used for recording measurement data [15]. The lenses  $L_1$  and  $L_2$  in the 4f configuration provides an accurate mapping of the object wave field to the parallel observation (sensor) plane. An optical mask with the complex-valued transmittance  $M_r$ , located at the Fourier plane (a phase modulating SLM) enables linear filter operations.

strongest sources of disturbances is the used SLM due to a high sensitivity of 4f system to modulation of the wave field at the Fourier plane.

In general, there are diversity of numerical approaches, which are used for calibration [16], filtering parasitic reflections [17], compensating for curvature introduced by microscope objective [18, 19], for aberrations [20] or astigmatism [21]. In this work we follow an essentially different idea. It is assumed that there is a *generalized pupil function* [14, §6.4.1] at the object plane which describes aberrations in the coherent imaging system manifested at the sensor plane. Namely, we do not try to identify particular sources of the disturbances but estimate and compensate their accumulated effects by recalculating them to the entrance pupil of the used 4f configuration. In the following, the cumulative distortions are referred to as “background” distortions. Thus, we are developing two step phase-retrieval algorithm: firstly, we estimate this background disturbance using special calibration experiments and then use it to reconstruct the object amplitude and phase. In this work we apply the variational constrained maximum likelihood formulation with parallel processing of multiple intensity observations proposed in our previous works [22, 23, 24, 25]. Moreover, we incorporate prior information on the true object wave field: in our experiments we reconstruct a binary object with unknown lower and upper levels.

Let  $u_0(x)$ ,  $x \in R^2$  be a true object wave field at the entrance pupil of the system. Taking into consideration the non-ideality of the optical system, we introduce a “disturbed” object wave field  $\tilde{u}_0(x)$  as a product of a typically unknown background (cumulative distortion) wave field  $u_B$  by the true

object wave field  $u_0(x)$  as

$$\tilde{u}_0(x) = u_0(x) \cdot u_B(x), \quad (1)$$

where the diacritic  $\sim$  emphasizes the difference of the corrupted wave field  $\tilde{u}_0$  from the ideal one  $u_0$ . The standard phase-retrieval techniques are able to give the reconstruction of the disturbed wave field  $\tilde{u}_0(x)$  only and they are not able to separate the background in order to estimate the true wave field  $u_0(x)$ .

In our work, we try to reconstruct the disturbances by performing a calibration procedure (to estimate the background  $u_B$ ) and use it to extract the true object  $u_0$ . At first glance, this problem looks trivial: one may produce the experiments with a known invariant  $u_0(x)$ , for instance  $u_0(x) = 1$ , obtain the estimate  $\hat{u}_B(x)$  and then recalculate the estimate for the object as  $\hat{u}_0(x) = \tilde{u}_0(x)/\hat{u}_B(x)$ . However, a priori information about the object in the used sparse modeling concerns the true object wave field  $u_0$  but not the disturbed one  $\tilde{u}_0$ . Thus, we are processing the recalculated object estimate at each iteration ( $\hat{u}_0^t(x) = \tilde{u}_0^t(x)/\hat{u}_B(x)$ ,  $t = 0, 1, 2, \dots$ ), and the structure of the developed iterative phase-retrieval algorithm is therefore essentially different from the trivial guess.

The paper is organized as follows. In Section 2, the image formation in a 4f optical system and the observation model are presented. The constrained variational approach for the phase retrieval and the sparse modeling for the object phase and amplitude are introduced in Section 3. The proposed phase-retrieval algorithm with the background compensation is presented in Section 4. Numerical experiments for the object wave field reconstructions from real data are shown and discussed in details in Section 5.

## 2. OBSERVATION MODEL

Let us consider the image formation model in a conventional 4f configuration of the coherent imaging system linking complex amplitudes at the object and measurement planes.

Let us denote complex amplitudes at the object and measurement (sensor) planes by  $u_0(x)$  and  $u_r(y)$ , respectively. The lenses  $L_1$  and  $L_2$  with the focal length  $f$  arranged in the 4f configuration provides an accurate mapping of the object wave field into the parallel measurement plane. A reflective phase modulating spatial light modulator (SLM) is placed at the Fourier plane of the first lens [15]. The used 4f optical system is illustrated in Fig. 1.

Let us assume for a moment that there are no distortions in the optical track. It is well known that the link between the wave fields at the object  $u_0(x)$  and the Fourier planes  $u_F(\frac{v}{\lambda f})$  is given as follows [14]

$$u_F(\frac{v}{\lambda f}) = \frac{1}{i\lambda f} \mathcal{F}\{u_0(x)\}(\frac{v}{\lambda f}), \quad (2)$$

where  $\mathcal{F}\{\cdot\}$  denotes the 2D integral Fourier transform,  $\lambda$  is a wavelength.

If the optical mask (SLM) inserted at the Fourier plane has the complex-valued transmittance  $M_r(\frac{v}{\lambda f})$ , then the output of the optical system is defined as

$$u_r(y) = \frac{1}{i\lambda f} \mathcal{F}\{u_F(\frac{v}{\lambda f}) \cdot M_r(\frac{v}{\lambda f})\}(-y). \quad (3)$$

All these wave field distributions are given in the 2D lateral coordinates: here we use the variables  $x, y, v \in \mathbb{R}^2$  for the object, sensor and Fourier planes, respectively.

## 2.1. Discrete modeling

For discrete modeling, the continuous arguments are replaced by the digital ones with a corresponding replacement of the continuous functions by their discrete counterparts:  $u_0(x) \rightarrow u_0(k_1\Delta_{x_1}, k_2\Delta_{x_2})$ ,  $u_r(y) \rightarrow u_r(l_1\Delta_{y_1}, l_2\Delta_{y_2})$ ,  $u_F(\frac{v}{\lambda f}) \rightarrow u_F(\frac{\Delta_{v_1}}{\lambda f}\eta_1, \frac{\Delta_{v_2}}{\lambda f}\eta_2)$  with 2D integer arguments  $k = (k_1, k_2)$ ,  $l = (l_1, l_2)$  and  $\eta = (\eta_1, \eta_2)$ . This discretization is dictated by the use of a digital camera and a pixelated SLM as a 2D array of liquid crystal cells. Thus, we hereafter consider the discrete wave fields at the object  $u_0[k_1, k_2]$ , Fourier  $u_F[\eta_1, \eta_2]$  and sensor planes  $u_r[l_1, l_2]$  with various pixel sizes  $\Delta_{x_1} \times \Delta_{x_2}$ ,  $\Delta_{v_1} \times \Delta_{v_2}$  and  $\Delta_{y_1} \times \Delta_{y_2}$ , respectively. In general, these images can be rectangular of different size  $N_{x_1} \times N_{x_2}$ ,  $N_{v_1} \times N_{v_2}$  and  $N_{y_1} \times N_{y_2}$ , respectively.

We use a vector-matrix notation for complex-valued distributions of the wave fields. 2D discrete distributions (matrices) are vectorized to the complex-valued column vector [26]. Bold lower case characters are used for the vectors. Matrices are defined by bold upper case to distinguish them from vectors. Thus,  $\mathbf{u}_0[k]$ ,  $\mathbf{u}_F[\eta]$  and  $\mathbf{u}_r[l]$  are column vectors constructed by vectorization of the corresponding 2D discrete wave field distributions at the object  $\mathbf{U}_0[k_1, k_2]$ , Fourier  $\mathbf{U}_F[\eta_1, \eta_2]$  and sensor planes  $\mathbf{U}_r[l_1, l_2]$ , respectively.

In this work we assume that the pixel size at the object and sensor planes is the same ( $\Delta_{x_1} = \Delta_{y_1}$ ,  $\Delta_{x_2} = \Delta_{y_2}$ ) and images  $\mathbf{U}_0$ ,  $\mathbf{U}_F$  and  $\mathbf{U}_r$  are of the same size  $N_x \times N_y$  for all planes. Let us also assume that the following conditions are fulfilled [27]

$$\Delta_{v_1}\Delta_{x_1}N_x = \lambda f, \Delta_{v_2}\Delta_{x_2}N_y = \lambda f \quad (4)$$

Then, discretization of the integral in Eq. (2) defines  $\mathbf{U}_F[\eta_1, \eta_2]$  as 2D discrete Fourier transform (DFT) of  $\mathbf{U}_0[k_1, k_2]$  in the form

$$\begin{aligned} \mathbf{U}_F[\eta_1, \eta_2] = & \quad (5) \\ & \frac{\Delta_{x_1}\Delta_{x_2}}{i\lambda f} \sum_{k_1=-\frac{N_{x_1}}{2}}^{\frac{N_{x_1}}{2}-1} \sum_{k_2=-\frac{N_{x_2}}{2}}^{\frac{N_{x_2}}{2}-1} \mathbf{U}_0(k_1\Delta_{x_1}, k_2\Delta_{x_2}) \times \\ & \times \exp\left(\frac{2\pi}{i\lambda f} \cdot (\eta_1\Delta_{v_1}k_1\Delta_{x_1} + \eta_2\Delta_{v_2}k_2\Delta_{x_2})\right) \\ & -\frac{N_{v_1}}{2} \leq \eta_1 \leq \frac{N_{v_1}}{2} - 1, -\frac{N_{v_2}}{2} \leq \eta_2 \leq \frac{N_{v_2}}{2} - 1 \end{aligned}$$

Similarly, discrete model for Eq.(3) has the form

$$\mathbf{U}_r[l_1, l_2] = \frac{\Delta_{v_1}\Delta_{v_2}}{i\lambda f} F\{\mathbf{U}_F \circ \mathbf{M}_r\}[-l_1, -l_2] \quad (6)$$

where  $F\{\cdot\}$  in Eqs. (5) and (6) denotes the 2D DFT operator.  $\circ$  stands for the Hadamard (elementwise) product and  $\mathbf{M}_r[\eta_1, \eta_2]$  is the discretized optical mask at the Fourier plane. Note that the wave field propagation can be easily realized much faster using FFT (cf. [24, 25]).

Taking into account the vector-matrix notation and the distortions in the real optical system (Eq. (1)), the forward wave field propagation from the object to the sensor plane can be given in the form

$$\mathbf{u}_r = \mathbf{A}_r \cdot \tilde{\mathbf{u}}_0, r = 1, \dots, K, \quad (7)$$

where  $\tilde{\mathbf{u}}_0 \in \mathbb{C}^{n \times 1}$  is a complex-valued vector, corresponding to the disturbed object discrete 2D wave field distribution,  $n = N_x \cdot N_y$ .  $\mathbf{A}_r \in \mathbb{C}^{n \times n}$  is a forward propagation operator corresponding to the optical mask  $\mathbf{M}_r$  at the Fourier plane (programmed using the SLM), and  $K$  is a number of these various optical masks.

## 2.2. Noisy intensity observations

Assume that we have a set of  $K$  experiments produced with different masks  $\{\mathbf{M}_r\}_r$ ,  $r = 1, \dots, K$ . The problem is to reconstruct a complex-valued true object wave field  $\mathbf{u}_0$  from multiple noisy intensity observations  $\{\mathbf{o}_r\}$  measured at the sensor plane. These measurements are represented in the vector-matrix notation following to Eq. (7) as follows

$$\mathbf{o}_r[l] = |\mathbf{u}_r[l]|^2 + \varepsilon_r[l], r = 1, \dots, K, \quad (8)$$

where the noise is assumed to be zero-mean Gaussian with the variance  $\sigma_r^2$ ,  $\varepsilon_r[l] \sim \mathcal{N}(0, \sigma_r^2)$ , independent for different  $l$  and  $r$ . The observation vectors  $\{\mathbf{o}_r\}$  correspond to the 2D distributions on the regular discrete grid located at the sensor plane.

## 3. SPARSE OBJECT MODELING AND VARIATIONAL FORMULATION

It is assumed in sparse modeling approach that the “true” object distribution  $\mathbf{u}_0$  can be approximated by a small number of non-zero elements of basis functions. The ideal basis functions for the object approximation are unknown a priori and selected from a given set of potential bases (dictionaries). In general, we deal with a complex-valued object wave field, and hence consider nonlinear modeling of the wave field with separate approximations for the object phase and amplitude [22, 23, 24, 25]. We represent the object wave field in the form  $\mathbf{u}_0 = \mathbf{a}_0 \circ \exp(j \cdot \varphi_0)$ , where  $\mathbf{a}_0 \triangleq \text{abs}(\mathbf{u}_0) \in \mathbb{R}^n$  and  $\varphi_0 \triangleq \text{angle}(\mathbf{u}_0) \in \mathbb{R}^n$  denote the object amplitude and

phase, respectively. Sparse object approximation can be given in the analysis or synthesis form as follows

$$\begin{aligned}\theta_a &= \Phi_a \cdot \text{abs}(\mathbf{u}_0), \theta_\varphi = \Phi_\varphi \cdot \text{angle}(\mathbf{u}_0) & (\text{analysis}) \\ \mathbf{a}_0 &= \Psi_a \cdot \theta_a, \varphi_0 = \Psi_\varphi \cdot \theta_\varphi & (\text{synthesis})\end{aligned}\quad (9)$$

Here  $\Psi_a, \Psi_\varphi$  and  $\Phi_a, \Phi_\varphi$  are the frame transform matrices, and the vector  $\theta_a, \theta_\varphi \in \mathbb{R}^m$  can be considered as a spectrum ( $m \gg n$ ) in a parametric data adaptive approximation. Subindices  $a$  and  $\varphi$  are shown for the amplitude and phase, respectively. It is recognized that, in contrast to classical orthonormal bases ( $m = n$ ), overcomplete frame based modeling is a much more efficient for imaging [28, 29] and results in a better wave field reconstruction accuracy. The sparsity of approximation is characterized by either the  $\ell_0$  norm  $\|\theta\|_0$  defined as a number of non-zero components of the vector  $\theta$  or the  $\ell_1$  norm as a sum of absolute values of components of the vector  $\|\theta\|_1 = \sum_s |\theta_s|$ . A smaller value of the norm means a higher sparsity of approximation. Note that results obtained by  $\ell_0$  or  $\ell_1$  norms are shown to be closed to each other [30], what allows replacing the nonconvex  $\ell_0$  norm by the convex  $\ell_1$  norm in many variational settings.

The main intention is to find sparsest (shortest) models for phase and amplitude with smallest values of the  $\ell_0$  or  $\ell_1$  norms. The separate sparse modeling for the object phase and amplitude is realized via the powerful BM3D-frame filter, specified for denoising and other imaging problems [31, 32, 33].

Assume that the background wave field  $\mathbf{u}_B$  is given. Taking into account the sparse modeling for the object amplitude and phase, the wave field reconstruction is performed by minimization of the criterion  $\mathcal{J}$

$$\mathcal{J} = \sum_{r=1}^K \frac{1}{2\sigma^2} \|\mathbf{o}_r - |\mathbf{u}_r|^2\|_2^2 + \tau_a \|\theta_a\|_p + \tau_\varphi \|\theta_\varphi\|_p \quad (10)$$

$$\text{subject to } \mathbf{u}_r = \mathbf{A}_r \cdot \tilde{\mathbf{u}}_0, r = 1, \dots, K, \quad (11)$$

$$\tilde{\mathbf{u}}_0 = \mathbf{u}_0 \circ \mathbf{u}_B \quad (12)$$

$$\theta_a = \Phi_a \cdot \text{abs}(\mathbf{u}_0), \theta_\varphi = \Phi_\varphi \cdot \text{angle}(\mathbf{u}_0), \quad (13)$$

$$\mathbf{a}_0 = \Psi_a \cdot \theta_a, \varphi_0 = \Psi_\varphi \cdot \theta_\varphi \quad (14)$$

where  $\|\cdot\|_2$  stands for the Euclidean norm and regularization terms for phase and amplitude are taken using the  $\ell_p$  norms ( $p = \{0, 1\}$ ). The positive parameters  $\tau_a$  and  $\tau_\varphi$  in Eq. (10) define a balance between the fit of observations, smoothness of the wave field reconstruction and the complexity of the used model (cardinality of spectra  $\theta_a, \theta_\varphi$  of the object amplitude and phase). Note that the constraint for the forward wave field propagation (11) is presented for the disturbed object wave field  $\tilde{\mathbf{u}}_0$  (Eq. (12)), and the used sparse modeling is given for the true object: namely, the analysis (13) and synthesis (14) are calculated using the frame transform matrices for the compensated object  $\mathbf{u}_0[k] = \tilde{\mathbf{u}}_0[k]/\mathbf{u}_B[k]$  (rather for the object amplitude and phase).

### 3.1. Multi-objective optimization

It is shown in [33] that a multi-objective optimization can be much more efficient than the minimization of the single criterion  $\mathcal{J}$  due to a simpler implementation (filtering and inverse procedure are decoupled) and resulting better reconstruction quality. Thus, instead of the constrained minimization of (10) we arrive at the unconstrained minimization of two criterion functions  $\mathcal{J}_1$  and  $\mathcal{J}_2$  with changing the constraints for sparse modeling by the quadratic penalties with positive weights

$$\begin{aligned}\mathcal{J}_1 &= \frac{1}{\gamma_0} \|\tilde{\mathbf{u}}_0 - \tilde{\mathbf{v}}_0\|_2^2 + \quad (15) \\ &+ \sum_{r=1}^K \frac{1}{\sigma^2} \left[ \frac{1}{2} \|\mathbf{o}_r - |\mathbf{u}_r|^2\|_2^2 + \frac{1}{\gamma_r} \|\mathbf{u}_r - \mathbf{A}_r \cdot \tilde{\mathbf{u}}_0\|_2^2 + \right. \\ &\quad \left. + \frac{2}{\gamma_r} \text{Re}\{\Lambda_r^H \cdot (\mathbf{u}_r - \mathbf{A}_r \cdot \tilde{\mathbf{u}}_0)\} \right],\end{aligned}$$

$$\begin{aligned}\mathcal{J}_2 &= \tau_a \|\theta_a\|_p + \frac{1}{2\gamma_a} \|\theta_a - \Phi_a \cdot \text{abs}(\mathbf{u}_0)\|_2^2 + \quad (16) \\ &+ \tau_\varphi \|\theta_\varphi\|_p + \frac{1}{2\gamma_\varphi} \|\theta_\varphi - \Phi_\varphi \cdot \text{angle}(\mathbf{u}_0)\|_2^2,\end{aligned}$$

where  $(\cdot)^H$  stands in Eq. (15) for the Hermitian conjugate,  $\mathbf{v}_0 = \Psi_a \theta_a \circ \exp(j \cdot \Psi_\varphi \theta_\varphi)$  is an approximation of the complex-valued object distribution  $\mathbf{u}_0$ ,  $\tilde{\mathbf{v}}_0 = \mathbf{v}_0 \circ \mathbf{u}_B$ .  $\{\Lambda_r\} \in \mathbb{C}^n$  are the complex-valued vectors of the Lagrange multipliers (see [34]). Note that the linear and quadratic penalties related to the forward propagation are involved with the same positive parameters  $\gamma_r$ . The analysis and synthesis constraints in Eqs. (13) and (14) are replaced by the penalties with the corresponding positive parameters  $\gamma_a, \gamma_\varphi$  and  $\gamma_0$ , in Eqs. (15) and (16), what is a standard tools to deal with constrained optimization [35].

Note that the criterion function  $\mathcal{J}_2$  is separable with respect to  $\theta_a$  and  $\theta_\varphi$ , thus it can be rewritten as  $\mathcal{J}_2 = \mathcal{J}_{2,a} + \mathcal{J}_{2,\varphi}$ , where

$$\mathcal{J}_{2,a}(\theta_a, \text{abs}(\mathbf{u}_0)) = \quad (17)$$

$$\begin{aligned}&= \tau_a \cdot \|\theta_a\|_p + \frac{1}{2\gamma_a} \|\theta_a - \Phi_a \cdot \text{abs}(\mathbf{u}_0)\|_2^2 \\ \mathcal{J}_{2,\varphi}(\theta_\varphi, \text{angle}(\mathbf{u}_0)) &= \quad (18) \\ &= \tau_\varphi \cdot \|\theta_\varphi\|_p + \frac{1}{2\gamma_\varphi} \|\theta_\varphi - \Phi_\varphi \cdot \text{angle}(\mathbf{u}_0)\|_2^2\end{aligned}$$

In contrast to [24], where only a quadratic penalization is used for the forward propagation model  $\mathbf{u}_r = \mathbf{A}_r \cdot \tilde{\mathbf{u}}_0$ , here we use the linear Lagrangian summand  $\text{Re}\{\Lambda_r^H \cdot (\mathbf{u}_r - \mathbf{A}_r \cdot \tilde{\mathbf{u}}_0)\}$  in Eq.(15). Thus,  $\mathcal{J}_1$  becomes the augmented Lagrangian objective function at least with respect to this particular constraint.



## 4. PROPOSED ALGORITHM

Following our assumption that the object wave field is degraded by the distortions accumulated in the background wave field  $\mathbf{u}_B$  ( $\tilde{\mathbf{u}}_0 = \mathbf{u}_0 \circ \mathbf{u}_B$ , cf. Eq. (1)), special calibration experiments are produced in order to estimate these disturbances. Thus, it is assumed that two sets of experiments are made consistently under the same conditions. These experiments result in two sets of observations  $\{\mathbf{o}_r^B\}$  and  $\{\mathbf{o}_r\}$  used to estimate the background  $\hat{\mathbf{u}}_B$  and the the object  $\mathbf{u}_0$ , respectively. The flowchart of the proposed two steps algorithm is shown in Fig. 2.

### 4.1. Background reconstruction

Firstly, we record a number of intensity observations  $\{\mathbf{o}_r^B\}$  corresponding to various optical masks  $\{\mathbf{M}_r\}$  for the free space object (test-image  $\mathbf{u}_0[k] = 1$ ) and find a complex-valued estimate  $\hat{\mathbf{u}}_B$  ( $\tilde{\mathbf{u}}_0 \equiv \mathbf{u}_B$ ) by optimization of the criterion function

$$\mathcal{J}_{AL} = \mu \|\mathbf{u}_B\|_2^2 + \sum_{r=1}^K \frac{1}{\sigma^2} \left[ \frac{1}{2} \|\mathbf{o}_r^B - |\mathbf{u}_r|^2\|_2^2 + \right. \quad (19)$$

$$\left. + \frac{1}{\gamma_r} \|\mathbf{u}_r - \mathbf{A}_r \mathbf{u}_B\|_2^2 + \frac{2}{\gamma_r} \text{Re}\{\Lambda_r^H (\mathbf{u}_r - \mathbf{A}_r \mathbf{u}_B)\} \right]$$

as it is described in [34]. The main difference of the structure of  $\mathcal{J}_{AL}$  from  $\mathcal{J}_1$  consists in the last quadratic penalty term.  $\mu$  in Eq. (19) is the Tikhonov regularization parameter which defines a balance between the prior information on  $\mathbf{u}_B$  and the fitting of calculated intensities  $|\mathbf{u}_r|^2$  to the given observations

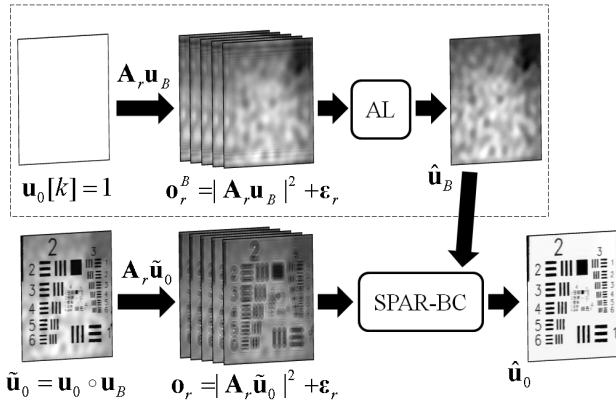


**Fig. 2.** A flowchart of the two steps phase retrieval technique with the background compensation. The upper block highlighted by a dashed line represents the background calibration procedure, where the complex-valued estimate of  $\mathbf{u}_B$  is found by *AL* [34]. The reconstruction of the object using the background estimate is obtained by the proposed *SPAR-BC* method.

$\mathbf{o}_r^B$ . The estimate  $\hat{\mathbf{u}}_B$  can be computed using the following algorithm

$$\begin{aligned} & \text{Repeat for } t = 0, 1, 2, \dots \quad (20) \\ & \text{Repeat for } r = 1, \dots, K \\ & \mathbf{u}_r^t = \arg \min_{\mathbf{u}_r} \mathcal{J}_{AL}(\mathbf{o}_r^B, \mathbf{u}_B^t, \mathbf{u}_r, \Lambda_r^t, ) \\ & \Lambda_r^{t+1} = \Lambda_r^t + \alpha_r \cdot (\mathbf{u}_r^t - \mathbf{A}_r \cdot \mathbf{u}_B^t) \\ & \text{End on } r \\ & \mathbf{u}_B^{t+1} = \arg \min_{\mathbf{u}_B} \mathcal{J}_{AL}(\{\mathbf{o}_r^B\}, \mathbf{u}_B, \{\mathbf{u}_r^t\}, \{\Lambda_r^t\}), \\ & \text{End on } t \end{aligned}$$

This algorithm without background compensation and additional object filtering is identical to the *AL* algorithm originated in [34] but presented with respect to the background  $\mathbf{u}_B$ .

This stage is shown in the upper block of Fig. 2 highlighted by a dashed line.

### 4.2. Object reconstruction

Secondly, we record intensity measurements for an object  $\{\mathbf{o}_r\}$  using the same optical masks  $\{\mathbf{M}_r\}$  as before and reconstruct the true object wave field using the found background estimate  $\hat{\mathbf{u}}_B$ .

According to the general idea of the multi-objective optimization, where the alternating minimization of  $\mathcal{J}_1$  with respect to  $\tilde{\mathbf{u}}_0 = \mathbf{u}_0 \circ \mathbf{u}_B$ ,  $\{\mathbf{u}_r\}$  and minimization of  $\mathcal{J}_2$  with respect to  $\theta_a, \theta_\varphi$  are used [32, 33, 24], we arrive at the following iterative algorithm

$$\mathbf{u}_0^t[k] = \tilde{\mathbf{u}}_0^t[k] / \hat{\mathbf{u}}_B[k] \quad (21)$$

$$\theta_a^t = \arg \min_{\theta_a} \mathcal{J}_{2,a}(\theta_a, \text{abs}(\mathbf{u}_0^t)) \quad (22)$$

$$\theta_\varphi^t = \arg \min_{\theta_\varphi} \mathcal{J}_{2,\varphi}(\theta_\varphi, \text{angle}(\mathbf{u}_0^t)) \quad (23)$$

$$\tilde{\mathbf{v}}_0^t = \Psi_a \theta_a^t \circ \exp(j \cdot \Psi_\varphi \theta_\varphi^t) \circ \hat{\mathbf{u}}_B \quad (24)$$

$$\mathbf{u}_r^t = \arg \min_{\mathbf{u}_r} \mathcal{J}_1(\mathbf{o}_r, \tilde{\mathbf{u}}_0^t, \mathbf{u}_r, \Lambda_r^t, \tilde{\mathbf{v}}_0^t), \quad (25)$$

$$\Lambda_r^{t+1} = \Lambda_r^t + \alpha_r \cdot (\mathbf{u}_r^t - \mathbf{A}_r \cdot \tilde{\mathbf{u}}_0^t), \quad r = 1, \dots, K, \quad (26)$$

$$\tilde{\mathbf{u}}_0^{t+1} = \arg \min_{\tilde{\mathbf{u}}_0} \mathcal{J}_1(\{\mathbf{o}_r\}, \tilde{\mathbf{u}}_0, \{\mathbf{u}_r^t\}, \{\Lambda_r^t\}, \tilde{\mathbf{v}}_0^t) \quad (27)$$

Here we first estimate the true object (Eq.(21)) by compensation of the disturbed  $\tilde{\mathbf{u}}_0^t$  with the background estimate  $\hat{\mathbf{u}}_B$ . It results in the object amplitude and phase estimates. Then, Eqs. (22) and (23) enable the spectrum estimates of the object amplitude and phase by thresholding in the BM3D-frame domain with the thresholds  $\tau_a \gamma_a$  and  $\tau_\varphi \gamma_\varphi$ , respectively [31, 32]. Eq. (24) corresponds to the synthesis of the approximation  $\tilde{\mathbf{v}}_0^t$  of the disturbed object from the calculated spectra for the true object amplitude and phase and using the background  $\hat{\mathbf{u}}_B$ . Together the operations in Eqs. (22)–(24) related to the optimization of  $\mathcal{J}_2$  can be rewritten in a more

compact form as follows

$$\begin{aligned} \mathbf{a}_0^{t+1/2} &= BM3D_a(abs(\mathbf{u}_0^t)), \\ \varphi_0^{t+1/2} &= BM3D_\varphi(angle(\mathbf{u}_0^t)), \\ \tilde{\mathbf{v}}_0^t &= \mathbf{a}_0^{t+1/2} \circ \exp(j \cdot \varphi_0^{t+1/2}) \circ \hat{\mathbf{u}}_B \end{aligned} \quad (28)$$

where  $BM3D(\cdot)$  denotes hereafter the processing by the BM3D filter, and the corresponding subindices  $a$  and  $\varphi$  emphasize that the filtering is performed with different parameters and different transform matrices  $\Psi$  and  $\Phi$  for the amplitude and phase, respectively. In our implementation the analysis and synthesis operations, the thresholding and calculation of the matrices  $\Psi$  and  $\Phi$  are integrated in a single block which is called *BM3D filter*.

Eqs. (25), (27) are the optimization steps for  $\mathcal{J}_1$ : the computation of the complex-valued wave field estimates  $\{\mathbf{u}_r\}$  at the sensor planes and the disturbed object  $\tilde{\mathbf{u}}_0$  from noisy intensity observations  $\{\mathbf{o}_r\}$ . The update of the Lagrange variables  $\Lambda_r$  is shown in Eq. (26). This second stage is illustrated in Fig. 2 under the mentioned block for the background estimation.

### 4.3. Sparse Phase Amplitude Reconstruction with Background Compensation (*SPAR-BC*)

Following the mentioned two main steps – Eqs. (20) for the background  $\hat{\mathbf{u}}_B$  estimation and Eqs. (21)–(27) for the true complex-valued object extraction – we formulate the advanced phase-retrieval approach with background compensation. Taking into account Eqs. (28), the reconstruction of the true object wave field is performed by the proposed iterative algorithm called **S**parse **P**hase **A**mplitude **R**econstruction with **B**ackground **C**ompensation (*SPAR-BC*).

The initialization concerns the calculation of the background (according to Eqs. (20)), the initial guess for the disturbed object  $\tilde{\mathbf{u}}_0^0 = \tilde{\mathbf{u}}_0^{init}$  (say, again by *AL* [34]) and Lagrange multipliers (e.g.  $\Lambda_r^0[k] = 0$ ). Note that the transform matrices for both the synthesis  $\Psi_a, \Psi_\varphi$  and analysis  $\Phi_a, \Phi_\varphi$  may be constructed only once during the initialization procedure or may be periodically updated. In this work we calculate these matrices only ones for the compensated object amplitude  $abs(\tilde{\mathbf{u}}_0^0[k])/abs(\hat{\mathbf{u}}_B[k])$  and phase estimates  $angle(\tilde{\mathbf{u}}_0^0[k]) - angle(\hat{\mathbf{u}}_B[k])$ . Note also that in our experiments we use the  $\ell_1$ -norm in the sparse object approximation (“soft” thresholding of the used BM3D filter, see [25, 33]).

Note that the output of the *SPAR-BC* phase-retrieval algorithm is not the estimate of the disturbed  $\tilde{\mathbf{u}}_0$  (Step 7), but the estimate of the true object wave field  $\mathbf{u}_0$  calculated in Step 1. The derivations of main steps of *SPAR-BC* (the minimization in Eqs. (22), (23), (25) and (27)) can be found in our previous works [34, 24, 25]. Step 4 returns the wave field  $\mathbf{u}_r^{t+1/2}$  at the sensor plane corresponding to the forward propagation model with the optical mask  $\mathbf{M}_r$ . Step 5 gives the updates of  $\mathbf{u}_r^{t+1/2}$  by their fitting to the observations  $\mathbf{o}_r$ . The

---

#### Algorithm: *SPAR-BC*

**Input:**  $\{\mathbf{o}_r\}_{r=1}^K, \{\mathbf{o}_r\}_{r=1}^K$

**Initialization:**  $\hat{\mathbf{u}}_B, \tilde{\mathbf{u}}_0^0, \{\Lambda_r^0\}$

**Repeat for**  $t = 0, 1, 2, \dots$

1. Object update (background compensation):

$$\mathbf{u}_0^t[k] = \tilde{\mathbf{u}}_0^t[k] / \hat{\mathbf{u}}_B[k]$$

2. BM3D filtering:

$$\mathbf{a}_0^{t+1/2} = BM3D_a(abs(\mathbf{u}_0^t)),$$

$$\varphi_0^{t+1/2} = BM3D_\varphi(angle(\mathbf{u}_0^t))$$

3. Object approximation synthesis:

$$\mathbf{v}_0^{t+1} = \mathbf{a}_0^{t+1/2} \circ \exp(j \cdot \varphi_0^{t+1/2})$$

**Repeat for**  $r = 1, \dots, K$

4. Forward propagation:

$$\mathbf{u}_r^{t+1/2} = \mathbf{A}_r \cdot \tilde{\mathbf{u}}_0^t$$

5. Fitting to observations:

$$\mathbf{u}_r^{t+1}[l] = \mathcal{G}(\mathbf{o}_r[l], \mathbf{u}_r^{t+1/2}[l], \Lambda_r^t[l]) \quad \forall l$$

6. Lagrange multipliers update:

$$\Lambda_r^{t+1} = \Lambda_r^t + \alpha_r \cdot (\mathbf{u}_r^{t+1} - \mathbf{u}_r^{t+1/2})$$

**End on**  $r$

7. Disturbed object update:

$$\begin{aligned} \tilde{\mathbf{u}}_0^{t+1} &= (\sum_{r=1}^K \frac{1}{\gamma_r \sigma_r^2} \mathbf{A}_r^H \mathbf{A}_r + \frac{1}{\gamma_0} \cdot \mathbf{I}_{n \times n})^{-1} \times \\ &\times \sum_{r=1}^K \frac{1}{\gamma_r \sigma_r^2} \mathbf{A}_r^H \cdot (\mathbf{u}_r^{t+1} + \Lambda_r^t) + \frac{1}{\gamma_0} \cdot (\hat{\mathbf{u}}_B \circ \mathbf{v}_0^{t+1}) \end{aligned}$$

**End on**  $t$

---

operator defining this update is denoted as  $\mathcal{G}$  and described in [34, Appendix A].

It is shown in [24] that the object reconstruction with BM3D filtering can be realized without Lagrange multipliers. However, it is found (see [25]) that  $\{\Lambda_r\}$  help to recover small details of the object. In Step 6  $\{\Lambda_r^t\}$  are updated with the step  $\alpha_r$ , and in our experiments we take a fixed step  $\alpha_r = \alpha = 1/20$  for all  $K$  observations.

In this work we use the same noise variation at all sensor planes ( $\sigma_r^2 = \sigma^2$ ) and take the equal parameters for the Lagrangian multipliers,  $\gamma_r = \gamma$ . Then, it is easy to see that the estimate  $\tilde{\mathbf{u}}_0^t$  computed in Step 7 of *SPAR-BC* consists of two parts: the disturbed object estimate calculated from the observations and the filtered object approximation found from the output of the BM3D filter. Then, this step of the algorithm can be given in the form

$$\tilde{\mathbf{u}}_0^{t+1} = \sum_{r=1}^K \mathbf{B}_r \cdot (\mathbf{u}_r^{t+1} + \Lambda_r^t) + \kappa \cdot \tilde{\mathbf{v}}_0^{t+1}, \quad (29)$$

where  $\tilde{\mathbf{v}}_0^{t+1} = \hat{\mathbf{u}}_B \circ \mathbf{v}_0^{t+1}$  and the transform matrix  $\mathbf{B}_r$  is given in the form

$$\mathbf{B}_r = (\sum_{r=1}^K \mathbf{A}_r^H \mathbf{A}_r + \kappa \cdot \mathbf{I}_{n \times n})^{-1} \mathbf{A}_r^H, \quad (30)$$

and  $\kappa = \gamma \sigma^2 / \gamma_0$ . In particular, for all our experiments  $\kappa$  is equal to  $90/25$ .

## 5. NUMERICAL RESULTS

In this Section a high performance of the proposed algorithm is demonstrated by example of amplitude reconstructions from real experimental data.

### 5.1. Binary object model

Here we consider reconstruction of a binary object with the amplitude given as

$$\mathbf{a}_0[k] = \text{abs}(\mathbf{u}_0[k]) = \begin{cases} \beta_1, & \text{for } k \in X_1 \subset X, \\ \beta_0, & \text{for } k \in X \setminus X_1, \end{cases} \quad (31)$$

where  $X$  is a support of the image,  $\beta_0 \in \mathbb{R}_+$  and  $\beta_1 \in \mathbb{R}_+$  stand for the lower and upper level of the object amplitude signal, respectively. The set  $X_1$  defines the indices of the upper level and the set  $X_0 = X \setminus X_1$  defines the indices of the lower level. Both the levels  $\beta_0, \beta_1$  and the sets  $X_0, X_1$  are unknown and should be reconstructed. The U.S. Air Force resolution test-chart is used for  $\mathbf{a}_0$ . For the amplitude-only object the phase should be equal to zero,  $\text{angle}(\mathbf{u}_0[k]) = 0$ . In practice, the laser beam passing through the chart undergoes some phase transformations. These transformations define the phase characteristics of the object  $\mathbf{u}_0$ , which are unknown. The only thing which can be stated is that the pattern of the object phase reflects the binary features of the amplitude model (31). Thus, we are looking for the complex-valued object  $\mathbf{u}_0$ .

### 5.2. Settings of parameters

The standard settings of the phase-retrieval problem assume a multi-plane lensless system with varying distances between the parallel object and sensor planes. The intensity measurements at the sensor planes are used for reconstruction of a 3D wave field including both the phase and amplitude. Following [15] the considered 4f optical system works as an imitator of this multi-plane lensless scenario. The principal difference is that the sensor plane is immobile and fixed at the distance  $4f$  from the object plane. The effect of the varying distances is obtained by a phase modulating SLM located at the Fourier plane, where different optical masks  $\mathbf{M}_r$  corresponding to the propagation distances are programmed as

$$\begin{aligned} \mathbf{M}_r[\eta_1, \eta_2] &= \\ &= \exp(2i \frac{\pi}{\lambda} z_r \sqrt{1 - \Delta_{v_1}^2 \frac{|\eta_1|^2}{f^2} - \Delta_{v_2}^2 \frac{|\eta_2|^2}{f^2}}) \end{aligned} \quad (32)$$

In Eq. (32)  $z_r = z_1 + (r - 1) \cdot \Delta_z$ ,  $r = 1, \dots, K$  are the distances between the object and sensor planes. In our experiments  $K=5$ ,  $z_1=20\text{mm}$  is the distance from the object to the first measurement plane,  $\Delta_z=2\text{mm}$  is the fixed distance between successive measurement planes.

Due to the bandlimitedness (fixed size of the SLM) and discrete representation of the optical mask (on a 2D array of liquid crystal cells of the SLM), the experimental results at the sensor plane will be different from the output of the model calculated using the angular spectrum decomposition (ASD, [14]). These differences are considered as components of the background to be estimated and compensated.

In our discrete wave field propagation model, the pixels at the sensor and Fourier planes are square of the different size  $\Delta_{y_1} \times \Delta_{y_1} = 3.45 \times 3.45 \text{ } (\mu\text{m})$  and  $\Delta_{v_1} \times \Delta_{v_2} = 8 \times 8 \text{ } (\mu\text{m})$ , respectively, with 100% fill factor [36, 37]. The object is pixelated with the sensor size pixels:  $\Delta_{x_1} = \Delta_{x_2} = \Delta_{y_1} = \Delta_{y_2}$ . The transparent U.S. Air Force resolution test-chart (MIL-STD-150A) inserted in the front focal plane of the first lens  $L_1$  is illuminated by collimated coherent light with wavelength  $\lambda=532 \text{ nm}$  (i.e. a green Nd:YAG laser is used). The employed SLM was supplied by Holoeye Photonics AG and configured to provide full  $2\pi$  phase modulation. The focal distance of lenses used in the 4f configuration is  $f=150 \text{ mm}$  what equates with the image size  $2892 \times 2892$  pixels according to the sampling conditions, Eq. (4). The measurement area is smaller and here we reconstruct only a part of the object of the size  $N_x \times N_y$  ( $2048 \times 2048$ ) for the corresponding computational focal distance  $f_c=106.25 \text{ mm}$  (see Eqs. (5)–(6)). Note that  $f=150 \text{ mm}$  in Eq. (32) defining the optical masks  $\mathbf{M}_r$ .

The algorithm is implemented for a graphic processing unit (GPU) in order to use the advantage of parallel processing of  $\mathbf{u}_r^{t+1}$  and  $\mathbf{u}_0^{t+1}$ . The GPU realization results in a significant acceleration what is crucial especially for large images [25]. The presented results are computed in MATLAB 7.13 (R2011b) using GPU Nvidia GF460GTX with CUDA 4.1. The computer used for experiments is Intel i5 2500 (4 physical cores) at 3.3 GHz; 8Gb RAM, Windows 7 SP1.

### 5.3. Modification of SPAR – BC for binary object

A special modification of the filtering procedure is developed targeted to improve reconstruction of a binary object. The BM3D filtering (Step 2 of SPAR – BC) is replaced by

$$\begin{aligned} \mathbf{a}_0^{t+1/3} &= \text{BM3D}_a(\text{abs}(\mathbf{u}_0^t) - \beta_0^t) + \beta_0^t \\ \mathbf{a}_0^{t+1/2} &= \text{BM3D}_a(\mathbf{a}_0^{t+1/3} - \beta_1^t) + \beta_1^t \end{aligned} \quad (33)$$

where  $\beta_0^t$  and  $\beta_1^t$  are scalar variables. These variables are calculated as medians of  $\mathbf{a}_0^t = \text{abs}(\mathbf{u}_0^t)$  over the sets:  $X_0^t = \{\mathbf{a}_0^t : 0 \leq \mathbf{a}_0^t \leq \rho^t\}$  and  $X_1^t = \{\mathbf{a}_0^t : \mathbf{a}_0^t > \rho^t\}$

$$\begin{aligned} \beta_0^t &= \text{median}_{\mathbf{a}_0^t \in X_0^t}(\mathbf{a}_0^t), \\ \beta_1^t &= \text{median}_{\mathbf{a}_0^t \in X_1^t}(\mathbf{a}_0^t) \end{aligned} \quad (34)$$

In order to estimate these classes  $X_0^t$  and  $X_1^t$ , corresponding to small and large values of  $\mathbf{a}_0^t$ , we use the thresholding parameter  $\rho^t$  calculated using the Otsu algorithm [38]. In the

procedures (33), successive subtractions of  $\beta_0^t$  and  $\beta_1^t$  makes the image flatter first in the area of low values of binary amplitude signal and after that in the area of its high values. Experiments show that this flattening enables much more efficient filtering of artifacts for the estimate of  $\mathbf{a}_0$  in case of binary object.

For the phase filtering we make the flattening procedure simpler because for the considered  $\mathbf{u}_0$  the phase should be close to zero. The median of the object phase is calculated only ones as  $\varphi_m^t = \text{median}(\text{angle}(\mathbf{u}_0^t))$  without partitioning in two subsets as for the object amplitude. Finally, the filtering procedure by the BM3D filter (Steps 2 and 3 in *SPAR-BC*) is replaced by the following ones

$$\begin{aligned} \mathbf{a}_0^{t+1/3} &= \text{BM3D}_a(\text{abs}(\mathbf{u}_0^t) - \beta_0^t) + \beta_0^t \\ \mathbf{a}_0^{t+1/2} &= \text{BM3D}_a(\mathbf{a}_0^{t+1/3} - \beta_1^t) + \beta_1^t \\ \varphi_0^{t+1/2} &= \text{BM3D}_\varphi(\text{angle}(\mathbf{u}_0^t) - \varphi_m^t) \\ \mathbf{v}_0^{t+1} &= \mathbf{a}_0^{t+1/2} \circ \exp(j \cdot (\varphi_0^{t+1/2} + \varphi_m^t)) \end{aligned} \quad (35)$$

The presented results of the object reconstruction from experimental data are obtained using this modification BM3D filtering.

#### 5.4. Initialization for *SPAR-BC*: reconstruction without background compensation

Here we consider the object reconstruction from the experimental data obtained by the approach originated in [15, 39]. The complex amplitude of the disturbed object is obtained by two various algorithm: by the mentioned *AL* algorithm [34] and by the successive phase-retrieval algorithm described in [40]. The second iterative algorithm is close to the circular wave reconstruction originated in [12, 13]: the calculated amplitude is replaced by the square root of the given noisy intensity, keeping the calculated phase (the initial guess for the phase is zero). For simplicity, we refer to the latter algorithm as the Falldorf-Agour (FA) algorithm.

In Fig. 3 we present the comparison of the reconstruction imaging of the disturbed object obtained from experimental data by these different methods. In the right column the estimate of the disturbed object phase and amplitude computed by the FA algorithm [40] are illustrated (see Fig. 3(b) and Fig. 3(d), respectively). In the left column the reconstructed disturbed object phase and amplitude found by *AL* [34] are shown (see Fig. 3(a) and Fig. 3(c), respectively). These results are shown for 25 iterations of the phase-retrieval algorithms. The artifacts which definitely should be addressed to the background are clearly seen in these images. It can be seen that the amplitude estimate by *AL* is significantly over-smoothed comparing with the result by FA. It is manifested in partial suppression of the diffraction artifacts on the geometrical elements with some degradation of a smooth surface as well. The phase reconstructions are not flat and have certain errors in the regions of the digits and geometrical figures in

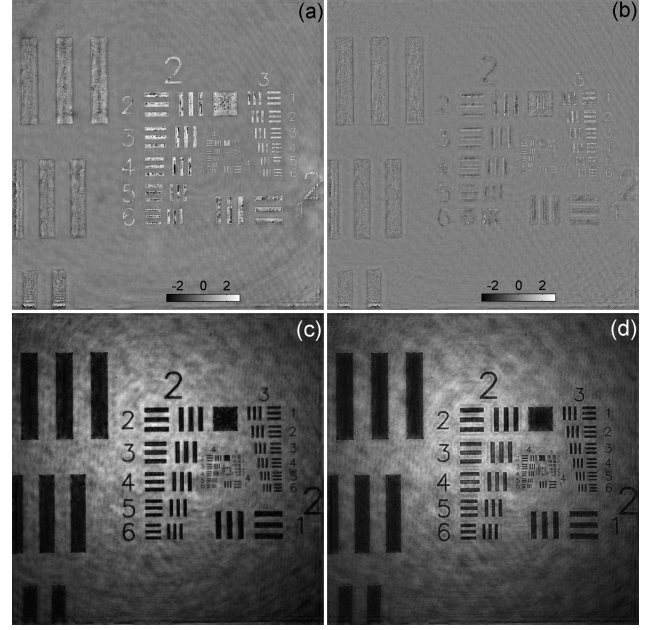


**Fig. 3.** Reconstructions of the “disturbed” object computed from experimental data (left column) by *AL* and (right column) by FA [40]. In the top row the amplitude reconstructions are presented: (a) by *AL*, (c) by FA. In the bottom row we demonstrate the phase estimates: (c) by *AL*, (d) by FA. The object reconstruction by *AL* ( $\tilde{\mathbf{a}}_0^0$  from (a) and  $\tilde{\varphi}_0^0$  from (c)) is used for the initialization  $\tilde{\mathbf{u}}_0^0 = \tilde{\mathbf{a}}_0^0 \circ \exp(j \cdot \tilde{\varphi}_0^0)$  in the *SPAR-BC* algorithm.

the amplitude. The phase by *AL* has stronger degradation of the phase comparing with the phase calculated by [40], because of a weak correction of the object reconstruction by Lagrange multipliers. We take quite small  $\alpha = 1/20$  because we are looking for a sharp result. It is found that larger  $\alpha$  may correct the phase estimate but leads to more noisy amplitude reconstruction, and denoising by larger regularization parameter  $\mu$  (see Eq. (19)) results in oversmoothing.

Note that the imperfect *AL* object estimate is used only as an initialization  $\tilde{\mathbf{u}}_0^0 = \tilde{\mathbf{a}}_0^0 \circ \exp(j \cdot \tilde{\varphi}_0^0)$  for the main procedure of *SPAR-BC*.

#### 5.5. *SPAR-BC*: reconstruction with background compensation

The background reconstruction is produced with the calibration experiments for the free space object  $\mathbf{u}_0[k] = 1$ . Figure 4(a) demonstrates the reconstructed background amplitude. However, the obtained results are appeared quite noisy and an additional postfiltering of the background amplitude  $\hat{\mathbf{a}}_B$  is introduced. Here we use the smoothed version of this background reconstruction with no high frequency components. For the filtering of the amplitude and the phase of  $\hat{\mathbf{u}}_B$  we



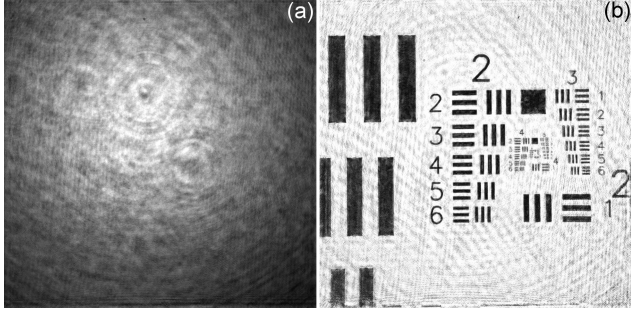


**Fig. 4.** Background compensation in *SPAR-BC*: (a) the reconstructed amplitude of the background  $abs(\hat{\mathbf{u}}_B)$  and (b) the initial guess for the object amplitude  $abs(\mathbf{u}_0^0)$  found with the smoothed background amplitude  $BM3D_a(abs(\hat{\mathbf{u}}_B))$ .

again use BM3D filter [32]. The cross-sections of the original  $\hat{\mathbf{a}}_B = abs(\hat{\mathbf{u}}_B)$  and smoothed  $\tilde{\mathbf{a}}_B = BM3D_a(\hat{\mathbf{a}}_B)$  background amplitudes are illustrated in Fig. 5. The result of the compensation of the initial object amplitude by such an smoothed background  $\mathbf{a}_0^0[k] = abs(\tilde{\mathbf{u}}_0^0[k])/\tilde{\mathbf{a}}_B[k]$  is shown in Fig. 4(b). The corresponding cross-section is presented in Fig. 8.

The results of the wave field reconstruction obtained by the developed *SPAR-BC* algorithm are shown in Fig. 6 for 25 iterations. In Figs. 6(a) and 6(b) the object amplitude reconstruction calculated with the smoothed and original background estimates are presented, respectively. It can be seen that the imaging of the amplitude estimate obtained using the smoothed background (Fig. 6(a)) is essentially better comparing with the reconstruction found with the background without postfiltering, namely: the artifacts are well seen of the border of Fig. 6(b). Further improvement of the imaging can be achieved by postfiltering of the reconstructed  $\hat{\mathbf{u}}_0$ , and in Fig. 6(c) the result of such an additional BM3D filtering of  $\hat{\mathbf{u}}_0$  (computed again with the smoothed  $\tilde{\mathbf{a}}_B$ ) is

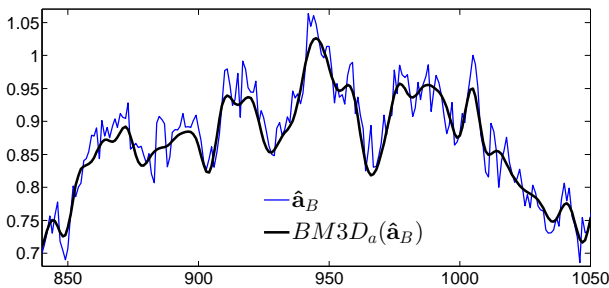


**Fig. 5.** Cross-sections of (thin curve) the amplitude estimate of the background,  $\hat{\mathbf{a}}_B = abs(\hat{\mathbf{u}}_B)$ , and (thick curve) its smoothed version computed by BM3D filter,  $BM3D_a(\hat{\mathbf{a}}_B)$ .

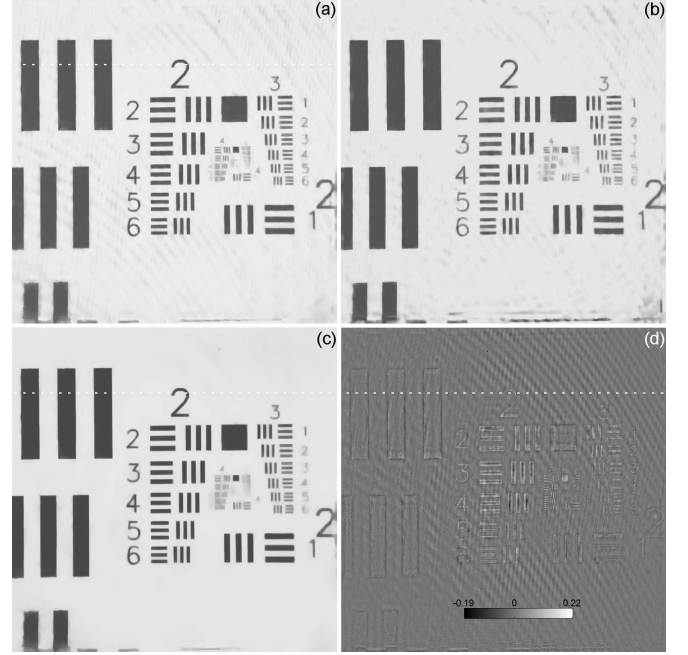


**Fig. 6.** Object reconstruction by *SPAR-BC*. Comparison of the reconstructed object amplitudes  $abs(\hat{\mathbf{u}}_0)$  calculated (a) with the smoothed background estimate and (b) with the original background reconstruction. The result of postfiltering of the object amplitude  $BM3D_a(abs(\hat{\mathbf{u}}_0))$ ,  $\tau_a\gamma_a = 0.04$ , is demonstrated in (c). The object phase estimate  $angle(\hat{\mathbf{u}}_0)$  is illustrated in (d). The noise in the filtered phase estimate is totally suppressed.

demonstrated. The reconstructed object phase  $angle(\hat{\mathbf{u}}_0)$  is illustrated in Fig. 6(d).

The threshold parameter of the BM3D filtering in *SPAR-BC* is  $\tau_a\gamma_a = 0.13$  for the object amplitude and  $\tau_\varphi\gamma_\varphi = 2$  for the phase. Note that even with a large thresholding

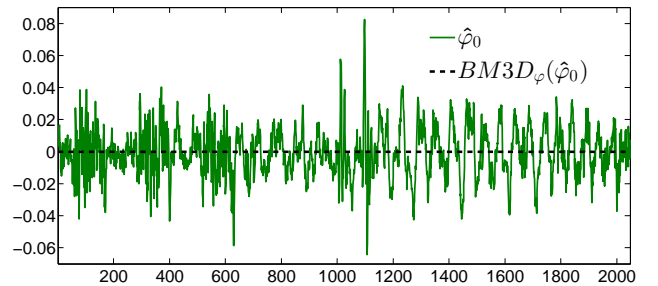


**Fig. 7.** Cross-sections of the reconstructed object phase  $\hat{\varphi}_0 = angle(\hat{\mathbf{u}}_0)$  and the filtered phase  $BM3D_\varphi(\hat{\varphi}_0)$ ,  $\tau_\varphi\gamma_\varphi = 0.08$ . These results are shown along the dashed lines shown in Fig. 6(d).

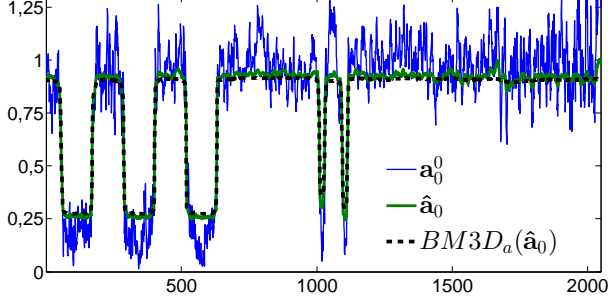


**Fig. 8.** Cross-sections of (solid thin curve) the initial guess  $\mathbf{a}_0^0 = \text{abs}(\mathbf{u}_0^0)$ , (solid thick) the reconstructed amplitude  $\hat{\mathbf{a}}_0 = \text{abs}(\hat{\mathbf{u}}_0)$  and (dashed curve) the filtered amplitude estimate  $\text{BM3D}_a(\hat{\mathbf{a}}_0)$ . These results are related to the imaging presented in Figs. 4(b), 6(a) and 6(c), respectively. The cross-sections are given along the dashed line in Fig. 6.

$\tau_\varphi \gamma_\varphi = 2$  we have significant noise in the phase estimate (see Fig. 6(d)). Taking into account that  $\varphi_0[k] = 0$ , the reconstruction accuracy for the phase is  $\text{RMSE}=0.2$ . However, we can completely wipe the phase noise out by the mentioned additional filtering by BM3D with quite a small  $\tau_\varphi \gamma_\varphi = 0.08$ : compare the cross-sections of  $\hat{\varphi}_0$  and  $\text{BM3D}_\varphi(\hat{\varphi}_0)$  in Fig. 7.

It is shown in Eq. (29) that the object reconstruction is a weighted sum of a noisy estimate from the propagation model and filtered approximation from the previous iteration. Thus, at each iteration the filtered object estimate is corrupted due to the used noisy intensity observations. It is a challenge to find a proper balance between denoising and oversmoothing. We obtain quite a sharp results of  $\hat{\mathbf{a}}_0$  with some small distortions (see Fig. 6(a) and the related cross-section in Fig. 8). However remaining noise and artifacts can be additionally suppressed by BM3D filter after the main procedure of *SPAR-BC*. It provides crisp imaging, but the resulting amplitude is over-smoothed and small details are almost lost: the result of post-filtering of  $\hat{\mathbf{a}}_0$  by 12 iterations with  $\tau_a \gamma_a = 0.04$  is presented in Fig. 6(c) and the corresponding cross-section in Fig. 8.

## 6. DISCUSSION AND CONCLUSION

It can be seen that the modified BM3D filtering (Eqs. (35)) works here as a classifier for the noisy binary object estimate. The estimate of the amplitude levels are found using the Otsu method, but the BM3D filtering shifts the value of the pixel  $\mathbf{a}_0^t[k]$  to one of these two levels  $\beta_0^t$  or  $\beta_1^t$  depending on the local neighborhood.

The result of classification is presented in Fig. 9. Let  $H(\cdot)$  stands for a histogram of a discrete distribution. The histogram  $H(\mathbf{a}_0^0)$  for the initial estimate of the compensated object amplitude is denoted in Fig. 9 by a solid curve. It is

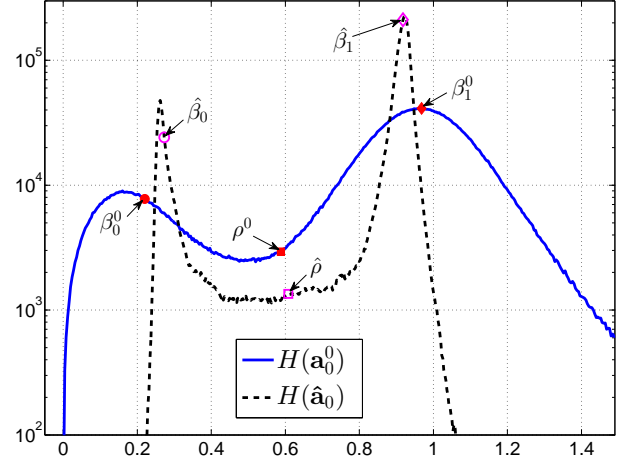


**Fig. 9.** Partition produced according to the modified BM3D filtering (Eqs. (35)). (solid curve)  $H(\mathbf{a}_0^0)$  is the histogram for the initial estimate of the object amplitude,  $\mathbf{a}_0^0 = \text{abs}(\mathbf{u}_0^0)$  presented in Fig. 4(b). (dashed curve)  $H(\hat{\mathbf{a}}_0)$  is the histogram for the resulting object amplitude estimate after 25 iterations,  $\hat{\mathbf{a}}_0 = \text{abs}(\hat{\mathbf{u}}_0)$  illustrated in Fig. 6(a). Otsu's threshold with the upper and lower levels of the initial  $(\rho^0, \beta_1^0, \beta_0^0)$  and resulting object estimates  $(\hat{\rho}, \hat{\beta}_1, \hat{\beta}_0)$  are also presented.

already seen that the object  $\mathbf{a}_0$  looks to be binary. The histogram of the resulting  $\hat{\mathbf{a}}_0$  is denoted here by a dashed curve. In Fig. 9 we also present the initial guess of the lower  $\beta_0^0$  and upper levels  $\beta_1^0$ , the resulting lower  $\hat{\beta}_0$  and upper levels  $\hat{\beta}_1$ , and the Otsu threshold for the initialization  $\rho^0$  and the final step  $\hat{\rho}$  of our reconstruction. Note that blurred regions (see small details and borders on the geometrical elements e.g. in Fig. 6(a)) correspond to a “sloping valley” between two peaks of  $H(\hat{\mathbf{a}}_0)$  in Fig. 9.

In this paper a novel phase-retrieval algorithm with background compensation and powerful BM3D filtering is presented. The *SPAR-BC* algorithm demonstrates a very good reconstruction quality: we have a clear separation of the binary true object, and the background estimate “undertakes” strong fluctuations, which would be difficult to compensate by filtering only. The reconstructions by two different phase-retrieval methods (*AL* and *FA*) are presented to emphasize the obtained enhancement of imaging of the developed algorithm with respect to modern phase-retrieval algorithms with no background compensation (compare the results in Figs. 3 and Fig. 6).

## 7. REFERENCES

- [1] R. W. Gerchberg and W. O. Saxton, “A practical algorithm for the determination of phase from image and diffraction plane pictures,” *Optik* **35**, 237–246 (1972).

- [2] D. L. Misell, "A method for the solution of the phase problem in electron microscopy," *J. Phys. D* **6**, L6–L9 (1973).
- [3] R. A. Gonsalves, "Phase retrieval from modulus data," *J. Opt. Soc. Am.* **66**, 961–964 (1976).
- [4] J. R. Fienup, "Reconstruction of an object from the modulus of its Fourier transform," *Opt. Lett.* **3**, 27–29 (1978).
- [5] B. Gu and G. Yang, "On the phase retrieval problem in optical and electronic microscopy," *Acta Opt. Sin.* **1**, 517–522 (1981).
- [6] G. Yang, B. Dong, B. Gu, J. Zhuang, and O. K. Ersoy, "Gerchberg-Saxton and Yang-Gu algorithms for phase retrieval in a nonunitary transform system: a comparison," *Appl. Opt.* **33**, 209–218 (1994).
- [7] Z. Zalevsky, D. Mendlovic, and R. Dorsch, "Gerchberg-Saxton algorithm applied in the fractional Fourier or the Fresnel domain," *Opt. Lett.* **21**, 842–844 (1996).
- [8] T. E. Gureyev, "Composite techniques for phase retrieval in the Fresnel region," *Opt. Commun.* **220**, 49–58 (2003).
- [9] J. R. Fienup, "Iterative method applied to image reconstruction and to computer generated holograms," *Opt. Eng.* **19**, 297–305 (1980).
- [10] J. R. Fienup, "Phase retrieval algorithms: a comparison," *Appl. Opt.* **21**, 2758–2769 (1982).
- [11] V. Yu. Ivanov, V. P. Sivokon, and M. A. Vorontsov, "Phase retrieval from a set of intensity measurements: theory and experiment," *J. Opt. Soc. Am. A* **9**, 1515–1524 (1992).
- [12] G. Pedrini, W. Osten, and Y. Zhang, "Wave-front reconstruction from a sequence of interferograms recorded at different planes," *Opt. Lett.* **30**, 833–835 (2005).
- [13] P. Almero, G. Pedrini, and W. Osten, "Complete wavefront reconstruction using sequential intensity measurements of a volume speckle field," *Appl. Opt.* **45**, 8596–8605 (2006).
- [14] J. W. Goodman, *Introduction to Fourier Optics*, 2nd ed. (McGraw-Hill, 1996).
- [15] C. Falldorf, M. Agour, C. v. Kopylow, and R. B. Bergmann, "Phase retrieval by means of a spatial light modulator in the Fourier domain of an imaging system," *Appl. Opt.* **49**, 1826–1830 (2010).
- [16] Q. Xue, Z. Wang, J. Huang, and J. Gao, "The elimination of the errors in the calibration image of 3D measurement with Structured Light," *Proc. SPIE* **8430**, (2012).
- [17] E. Cuhe, P. Marquet, and C. Depeursinge, "Spatial filtering for zero-order and twin-image elimination in digital off-axis holography," *Appl. Opt.* **39**, 4070–4075 (2000).
- [18] P. Ferraro, S. D. Nicola, A. Finizio, G. Coppola, S. Grilli, C. Magro, and G. Pierattini, "Compensation of the inherent wave front curvature in digital holographic coherent microscopy for quantitative phase-contrast imaging," *Appl. Opt.* **42**, 1938–1946 (2003).
- [19] G. Pedrini, S. Schedin, and H. J. Tiziani, "Aberration compensation in digital holographic reconstruction of microscopic objects," *J. Mod. Opt.* **48**, 1035–1041 (2001).
- [20] S. M. Zhao, J. Leach, L. Y. Gong, J. Ding, and B. Y. Zheng, "Aberration corrections for free-space optical communications in atmosphere turbulence using orbital angular momentum states," *Opt. Express* **20**, 452–461 (2012).
- [21] S. Grilli, P. Ferraro, S. D. Nicola, A. Finizio, G. Pierattini, and R. Meucci, "Whole optical wavefields reconstruction by digital holography," *Opt. Express* **9**, 294–302 (2001).
- [22] A. Migukin, V. Katkovnik, and J. Astola, "Advanced phase retrieval: maximum likelihood technique with sparse regularization of phase and amplitude," [arXiv:1108.3251v1](https://arxiv.org/abs/1108.3251).
- [23] V. Katkovnik and J. Astola, "High-accuracy wave field reconstruction: decoupled inverse imaging with sparse modeling of phase and amplitude," *J. Opt. Soc. Am. A* **29**, 44–54 (2012).
- [24] V. Katkovnik and J. Astola, "Phase retrieval via spatial light modulator phase modulation in 4f optical setup: numerical inverse imaging with sparse regularization for phase and amplitude," *J. Opt. Soc. Am. A* **29**, 105–116 (2012).
- [25] A. Migukin, V. Katkovnik, and J. Astola, "Advanced multi-plane phase retrieval using Graphic Processing Unit: augmented Lagrangian technique with sparse regularization," *Proc. SPIE* **8429**, (2012).
- [26] J. R. Magnus and H. Neudecker, *Matrix Differential Calculus with Applications in Statistics and Econometrics*, 2nd ed., (Wiley, 1999).
- [27] Th. Kreis, *Handbook of Holographic Interferometry: Optical and Digital Methods*, (Wiley-VCH, 2005).
- [28] M. Elad, *Sparse and Redundant Representations: From Theory to Applications in Signal and Image Processing* (Springer, 2010).
- [29] D. Han, K. Kornelson, D. Larson, and E. Weber, *Frames for Undergraduates* (Student Mathematical Library, AMS, 2007).
- [30] D. L. Donoho, "Compressed sensing," *IEEE Trans. Inf. Theory* **52**, 1289–1306 (2006).
- [31] V. Katkovnik, A. Danielyan, and K. Egiazarian, "Decoupled inverse and denoising for image deblurring: variational BM3D-frame technique," in *Proceedings of the International Conference on Image Processing (ICIP)*, 3514 – 3517 (2011).
- [32] A. Danielyan, V. Katkovnik, and K. Egiazarian, "Image deblurring by augmented Lagrangian with BM3D frame prior," in *Workshop on Information Theoretic Methods in Science and Engineering (WITMSE)*, Tampere, Finland, (2010).
- [33] A. Danielyan, V. Katkovnik, and K. Egiazarian, "BM3D frames and variational image deblurring," *IEEE Trans. on Image Proc.* **21**, 1715–1728 (2012).

- [34] A. Migukin, V. Katkovnik, and J. Astola, "Wave field reconstruction from multiple plane intensity-only data: Augmented Lagrangian algorithm", *J. Opt. Soc. Am. A* **28**, 993–1002 (2011).
- [35] D. P. Bertsekas, *Nonlinear Programming*, 2nd ed. (Athena Scientific, 1999).
- [36] V. Arrizon, E. Carreon, and M. Testorf, "Implementation of Fourier array illuminators using pixelated SLM: efficiency limitations," *Optics comm.* **16**, 207–213 (1999).
- [37] M. Agour, C. Falldorf, and C. von Kopylow, "Digital pre-filtering approach to improve optically reconstructed wave-fields in opto-electronic holography," *J. Opt.* **12**, 055401 (2010).
- [38] N. Otsu. "A threshold selection method from gray-level histograms," *IEEE Transactions of Systems, Man and Cybernetics* **9**, 62–66 (1979).
- [39] M. Agour, C. Falldorf, C. v. Kopylow, R. B. Bergmann, "Automated compensation of misalignment in phase retrieval based on a spatial light modulator," *Appl. Opt.* **50**, 4779-4787 (2011).
- [40] M. Agour, C. Falldorf, C. von Kopylow and R. B. Bregmenn, "The effect of misalignment in phase retrieval based on a spatial light modulator," *Proc. SPIE* **8082**, (2011).